

Article

Thymus saturooides Oil as Green Corrosion Inhibitor for 316L Stainless Steel in 3% NaCl: Experimental and Theoretical Studies

Florica Simescu-Lazar¹, Soukaina Slaoui², Mohamed Essahli², Frédéric Bohr¹, Abdeslam Lamiri², Laurent Vanoye³  and Jean Paul Chopart^{1,*}

¹ MATIM Laboratory, University of Reims Champagne-Ardenne, 51687 Reims, France

² Laboratory of Applied Chemistry and Environment, Faculty of Science and Technology, University Hassan 1er, Settlat 26002, Morocco

³ Université Lyon, Catalyse Polymérisation Procédés & Matériaux (CP2M), CNRS – CPE Lyon, 43 boulevard du 11 novembre 1918, F-69100 Villeurbanne, France

* Correspondence: jean-paul.chopart@univ-reims.fr

Abstract: The protection of 316L stainless steel in 3% NaCl by the essential oil of *Thymus saturooides* has been studied by many techniques such as potentiodynamic polarization, electrochemical impedance spectroscopy (EIS), atomic force microscopy (AFM) and scanning electron microscopy (SEM) coupled with energy dispersive X-ray spectroscopy analysis (EDXS). The results show that the corrosion rate of 316L stainless steel decreases with the increase in the concentration of the inhibitor up to an efficiency of 82% for a concentration of 1600 ppm. The *Thymus saturooides* oil acts as an anode inhibitor. The values of the inhibition effectiveness obtained from the polarization curves and electrochemical impedance spectroscopy (EIS) are in good agreement. Geometry optimization and calculation of the structural and electronic properties of the inhibitor molecular system have been carried out using density functional theory DFT (B3LYP, BMK and M062X) level with a 6-311++G** basis set.

Keywords: 316L stainless steel; green corrosion inhibitor; EIS; polarization; 3% NaCl solution; DFT calculation



Citation: Simescu-Lazar, F.; Slaoui, S.; Essahli, M.; Bohr, F.; Lamiri, A.; Vanoye, L.; Chopart, J.P. *Thymus saturooides* Oil as Green Corrosion Inhibitor for 316L Stainless Steel in 3% NaCl: Experimental and Theoretical Studies. *Lubricants* **2023**, *11*, 56. <https://doi.org/10.3390/lubricants11020056>

Received: 14 December 2022

Revised: 26 January 2023

Accepted: 30 January 2023

Published: 31 January 2023



Copyright: © 2023 by the authors. Licensee MDPI, Basel, Switzerland. This article is an open access article distributed under the terms and conditions of the Creative Commons Attribution (CC BY) license (<https://creativecommons.org/licenses/by/4.0/>).

1. Introduction

The corrosion of materials is one of the most important problems that represent a real ubiquitous danger for many industries. Various metals such as iron, aluminum, copper, magnesium, and their alloys are used in severe environments such as food, marine environment, aircraft applications, chemical industries, nuclear power plants etc. [1].

The metals and their alloys are also known for their physical characteristics, such as stiffness and high strength-to-weight ratios, but they are highly susceptible to corrosion in aggressive environments [2]. Among these alloys, there are stainless steels that are iron-based alloys with less than 0.3% carbon and at least 10.5% chromium by weight. For example, one of the major reasons for using stainless steel in many applications, is its good corrosion resistance in many aggressive environments which is attributed to the presence of a thin film of oxides [1] characterized by stability, sustainability and self-repair. However, these materials are susceptible to localized corrosion resistance in some aggressive environments and they can suffer from pitting corrosion in chloride environments [2–4].

The aggressiveness of chloride ions is due to their small size, their high diffusivity, their strong anionic nature and the very high solubility of many chloride salts. The study of the localized corrosion of stainless steels in chloride environments has high practical importance. The deterioration of the passive film by chloride ions with the priming of pitting appears at a critical potential called pitting potential (E_{pit}). It is one of the most

important parameters that characterize the sensitivity of the metals and alloys to pitting corrosion [3].

The use of inhibitors is one of the most practical ways to protect metals against corrosion. An inhibitor is generally added in small quantities in order to slow down the corrosion rate by adsorption mechanism [3,5]. Over the years, many inhibitors have been synthesized, these inhibitors contain one or several functional groups such as amine ($-\text{NH}-$), hydroxide ($-\text{OH}$), mercapto ($-\text{SH}$), phosphonate ($-\text{PO}_3\text{H}$), sulfonate ($-\text{SO}_3\text{H}$), carboxyl ($-\text{COOH}$) and their derivatives. However, these products are generally obtained by chemical synthesis, and therefore, they have a negative effect on the environment.

This has led many researchers around the world to use new natural molecules which are also nonpolluting for the environment, such as mentha spicata [6,7], perezona [8], jojoba oil [9], vanillin [10], olive leaf extract [11], licorice extract [12], chitosan [13], passiflora edulia Sims leaves extract [14] and food flavors [15]. The encouraging results obtained by these natural compounds as corrosion inhibitors for different metals and alloys [16–18] have encouraged us to examine the effect of the *Thymus satureoides* oil against the corrosion of 316L stainless steel in marine media (3% NaCl).

To the best of our knowledge, corrosion protection of 316L stainless steel in 3% NaCl using the *Thymus satureoides* oil, has not been carefully studied so far [19]. For this reason, the aim of the present work is to test the effectiveness of *Thymus satureoides* oil as a corrosion inhibitor for 316L stainless steel in a 3% NaCl solution by potentiodynamic polarization and electrochemical impedance spectroscopy methods. At the same time, the 316L stainless steel surfaces have been examined by atomic force microscopy (AFM) and scanning electron microscopy (SEM) coupled with energy dispersive X-ray spectroscopy (EDXS) analyses. Additionally, thermodynamic data were obtained from Arrhenius plots and theoretical calculation was carried out at the DFT level (B3LYP, BMK and M062X) with a 6-311++G** basis set.

2. Materials and Methods

2.1. Extraction of the *Thymus satureoides* Essential oil

The extraction of essential oil was obtained from the Morocco endemic *Thymus satureoides* by hydro-extractive steam distillation using a Clevenger distiller for 150 min. The yield of the essential oil, calculated on the basis of the dry matter, was 1.1%. The obtained oil was recovered and stored in a dark bottle at 4 °C before use. After extraction, a part of the oil was used for chemical composition analysis by gas chromatography (GC) coupled to mass spectroscopy (MS); the other part was used for the anti-corrosion study.

GC analyses were performed using a Shimadzu 2010 (Ipca Laboratories Limited, Mumbai, India) with MS detector for characterization and an Agilent 6890 (Agilent Scientific Instruments, Santa Clara, CA, USA) with FID detector for quantification. Both GC were equipped with DB-17MS column (10 m \times 0.1 mm \times 0.1 m), and a split injector; hydrogen was used as carrier gas.

2.2. Electrodes and Electrolyte

The material used for corrosion tests was commercial 316L stainless steel, whose chemical composition (wt%) is 0.023 C, 0.034 P, 0.004 S, 0.57 Si, 1.37 Mn, 2.05 Mo, 16.4 Cr, 10.3 Ni, 0.14 Cu, 0.039 N and Fe balance [20]. This chemical composition was verified by EDXS analyses.

The samples, in the form of a disc with a geometric area of 1.13 cm², were coated with epoxy resin to offer only one active flat surface exposed to the corrosive electrolyte. The working surface was polished mechanically by using different grades of emery paper (180, 600, 1200, 2400 and 4000) and then rinsed with deionized water and ethanol.

The electrolyte was freshly prepared, before each experiment, by the dissolution of NaCl powder (99.9%, Aldrich), in bi-distilled water. The *Thymus satureoides* essential oil concentration was taken in parts per million (ppm) for all investigations. Each experiment was conducted at least three times to ensure reliable and reproducible results. The experi-

ments were carried out in the absence and presence of inhibitors at various concentration ranges from 0 ppm to 1800 ppm and at different temperatures ranging from 25 °C to 80 °C.

2.3. Electrochemical Measurements

The electrochemical experiments were performed in a thermostated pyrex cell, equipped with conventional electrodes: stainless steel as the working electrode, platinum as the auxiliary electrode and a saturated calomel electrode (SCE) as the reference electrode. Before testing, the samples were allowed to reach the open circuit potential (OCP) in the test solution of 3% NaCl without and with the inhibitor for 120 min. The potentiodynamic polarization measurements were performed by scanning the applied potential from -800 mV vs. SCE to 600 mV vs. SCE, with a scan rate of 0.5 mVs $^{-1}$.

Electrochemical impedance spectroscopy (EIS) measurements were carried out at OCP using a PGZ potentiostat RADIOMETER 100. The frequency ranged from 10 kHz to 10 mHz with ten points per decade and an amplitude of 10 mV. EIS measurements were initiated about 120 min after the working electrode was introduced in the electrolyte to stabilize the steady-state potential. The impedance data were modeled using the ZSimpWin software.

The corrosion kinetic parameters such as corrosion potential (E_{corr}), corrosion current density (i_{corr}), and passivation current (i_{pass}) were calculated using VoltaMaster software 4. The percentage inhibition efficiency (EI%) was calculated from i_{corr} values using the relationship noted 1:

$$\text{EI}(\%) = \frac{i_{\text{corr}} - i'_{\text{corr}}}{i_{\text{corr}}} \times 100 \quad (1)$$

i_{corr} and i'_{corr} represent, respectively, the current corrosion densities at the corrosion potential without and with the inhibitor. These values have been determined by extrapolation using the Tafel method with a potential range of 100 mV around E_{corr} .

For electrochemical impedance, the inhibition efficiency $\text{EI}_{\text{EIS}}(\%)$ was evaluated from charge transfer resistance R_{ct} values using the following equation (noted 2):

$$\text{EI}_{\text{EIS}}(\%) = \frac{R'_{\text{ct}} - R_{\text{ct}}}{R'_{\text{ct}}} \times 100 \quad (2)$$

where R_{ct} and R'_{ct} are the charge transfer resistances of 316L in 3% NaCl without and with the addition of the inhibitor, respectively.

2.4. Surface Analysis

The surface morphology and average surface roughness of 316L stainless steel were analyzed by atomic force microscopy (AFM, Model Nanoscope III, Veeco, Plainview, NY, USA). Tapping mode images were obtained in air using Silicon tips coated with an aluminum reflective coating (Tap300Al-G) with a maximum radius of curvature equal to 10 nm and a spring constant $k = 40$ N/m. The scanned area is presented over a $1 \mu\text{m} \times 1 \mu\text{m}$ square.

A JSM-7900F Field Emission scanning electron microscope (Jeol, Tokyo, Japan) operating at 0 – 15 kV was used to observe the surface topography of 316L stainless steel with and without *Thymus satureoides* oil. This microscope fitted with a super hybrid lens (SHL) is also capable of electron energy selected imaging when combined with a new detection system consisting of two differently placed detectors: an upper electron detector (UED) and an upper secondary electron detector (USD), together with a filter located between SHL and UED.

For surface analysis, the 316L stainless steel specimens were polished mechanically, then immersed in the test solution without and with 1600 ppm inhibitor at 25 °C. After 24 h, the specimens were taken out from the solution, cleaned with distilled water, dried and used for AFM and SEM analysis.

2.5. Computational Details

Calculations were performed in the framework of density functional theory (DFT) using the GAUSSIAN09 package [21]. All calculations were conducted using the 6-311++G** basis set [22,23]. The B3LYP [24,25] hybrid functional as well as BMK [26] and M062X [27] functionals were used. Molecular structures were fully optimized using the analytical gradients. The default grid was used. It was a pruned (75,302) grid, having 75 radial shells and 302 angular points per shell, resulting in about 7000 points per atom. Calculations in solution were conducted using the Polarizable Continuum Model (PCM) [28]. The molecular frontier orbitals (HOMO—LUMO) and dipole moments of each molecule were calculated.

3. Results and Discussions

3.1. Chemical Composition of the Essential Oil

The essential oil chemical composition analysis has been carried out by GC-MS. The obtained chromatogram is represented in Figure S1 in the electronic Supplementary Material (SM). The retention time and the relative percentages of the essential oil's various components are presented in Table S1 (see the Supplementary Material). *Thymus satureoides* essential oil belongs to the areoles botany family and presents the following elements: borneol (13%), camphene (12%), p-cymene (12%), carvacrol methyl ether (10%), caryophyllene (9%) and 25 other detected compounds (Table S1). The essential oil chemical composition used in this study is similar to the published one by Houbairi et al. [29]. The chemical structure of the majority of the compounds (borneol, camphene, p-cymene and carvacrol methyl ether) is presented in Figure S2.

3.2. Open Circuit Potential

The potential evolution vs. time for 316L stainless steel in 3% NaCl solution with and without the inhibitor, during 120 min is presented in Figure S3.

Monitoring the open circuit voltage (OCV) saves the changes to the interface between the material and the environment. The evolution of the 316L free potential in 3% NaCl for 120 min, respectively, for each test concentration, shows that the inhibitor addition makes the steel nobler by the shift in the free potential to more positive values, which demonstrates the formation of a protective film which increases the corrosion resistance of stainless steel [30].

3.3. Potentiodynamic Polarization

The potentiodynamic polarization curves for 316L stainless steel in 3% NaCl with and without the addition of the green inhibitor are illustrated in Figure 1. The electrochemical parameters such as corrosion potential (E_{corr}), corrosion current density (i_{corr}), passivation current density (i_{pass}), pitting corrosion (E_{pit}) and the effectiveness of inhibition (EI%) are calculated and summarized in Table 1.

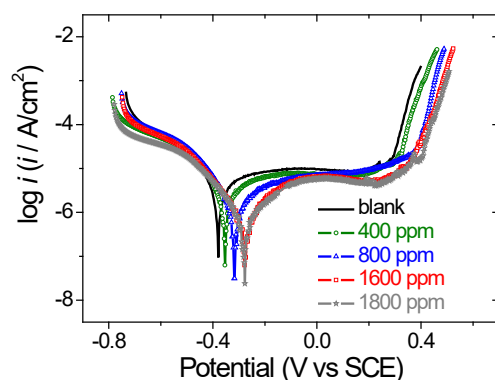


Figure 1. Potentiodynamic polarization curves (scan rate of 0.5 mVs^{-1}) for 316L stainless steel in 3% NaCl without and with inhibitor, at $25 \text{ }^\circ\text{C}$.

Table 1. Electrochemical parameters and the effectiveness of inhibition for 316L stainless steel after 2 h in 3% NaCl solution without and with inhibitor, at 25 °C, calculated from (a) potentiodynamic polarization curves (EI) and (b) electrochemical impedance measurements (EI_{EIS}). χ^2 is the error factor for the fitted values of the impedance measurements.

Inhibitor Conc. (ppm)	(a)					(b)					
	E_{corr} (V/SCE)	i_{corr} ($\mu\text{A}/\text{cm}^2$)	i_{pass} ($\mu\text{A}/\text{cm}^2$)	E_{pit} (V/SCE)	EI (%)	R_e ($\Omega\cdot\text{cm}^2$)	R_{ct} ($\text{k}\Omega\cdot\text{cm}^2$)	C_{dl} $\mu\text{F}/\text{cm}^2$	n	χ^2 (Error Factor)	EI _{EIS} (%)
Blank	−0.383	3.38	7.74	0.290		6.7	140	17.7	0.81	0.001	
400	−0.358	2.33	5.85	0.316	31	5.9	172	21.1	0.86	0.003	18
800	−0.323	0.95	5.87	0.376	73	6.2	337	11.5	0.84	0.001	58
≥1600	−0.287	0.62	5.55	0.380	82	6.1	972	4.8	0.87	0.005	86

From Figure 1 and Table 1 it is clear that the effectiveness of inhibition (EI%) increases with increasing concentration of *Thymus satureoides* oil to reach a maximum value of ~82% at a concentration equal to 1600 ppm and then remains constant for 1800 ppm.

This suggests that increasing the inhibitor concentration increases the number of molecules linked by adsorption on the surface, blocking the active sites and protecting the surface of the electrode. An inhibitor can be classified as anodic or cathodic if the difference between corrosion potentials (E_{corr}) is above 85 mV [31]. We note that the E_{corr} difference between 1600 ppm and blank samples is positive and equal to ~100 mV. This result indicates that this oil acts as an anodic-type inhibitor.

As we can see, it is clear that with increasing the concentration of *Thymus satureoides* oil, the differences between E_{corr} and E_{pit} , remain almost constant. Moreover, the passivation current density (i_{pass}) decreases by 25% to reach an almost constant value whatever the concentration of the inhibitor [32]. These results show that the oil is a good pitting inhibitor for the corrosion of 316L in a 3% NaCl solution.

3.4. Electrochemical Impedance Measurements

Electrochemical impedance spectroscopy (EIS) is one of the most helpful and revealing methods for metal corrosion measurements. It provides more information on both the resistive and capacitive behavior at the metal/solution interface and it is appropriate for in situ and non-destructively probing relaxation phenomena over a wide frequency range [33,34]. The measured impedance data are given as typical Nyquist and Bode plots.

EIS plots for different *Thymus satureoides* oil concentrations are represented in Figure 2a–c. All Nyquist curves (Figure 2a) appear to be similar with respect to their shape, but their amplitudes vary significantly. The Bode diagrams (Figure 2b) show one time constant at intermediate frequencies. Moreover, the impedance value increases with increasing the inhibitor concentration (Figure 2c). These results show that inhibitor adsorption occurs on a large surface of the electrode and the corrosion takes place on a very small fraction of the total stainless steel area.

The EIS spectra of all tests were analyzed using the electric equivalent circuit (EEC) shown in Figure 2d. This electric equivalent circuit is a parallel combination of the charge transfer resistance (R_{ct}) and the constant phase element (CPE), both in series with the electrolyte resistance (R_e). This type of electrochemical circuit was used previously to model the metal/inhibitor interface [35,36]. The electrochemical parameters such as electrolyte resistance, charge transfer resistance and CPE constants (Y_0 and n) were obtained from fitting the experimental data of Nyquist plots using ZView software 3.6 and the equivalent circuit is shown in Figure 2d and is presented in Table 1.

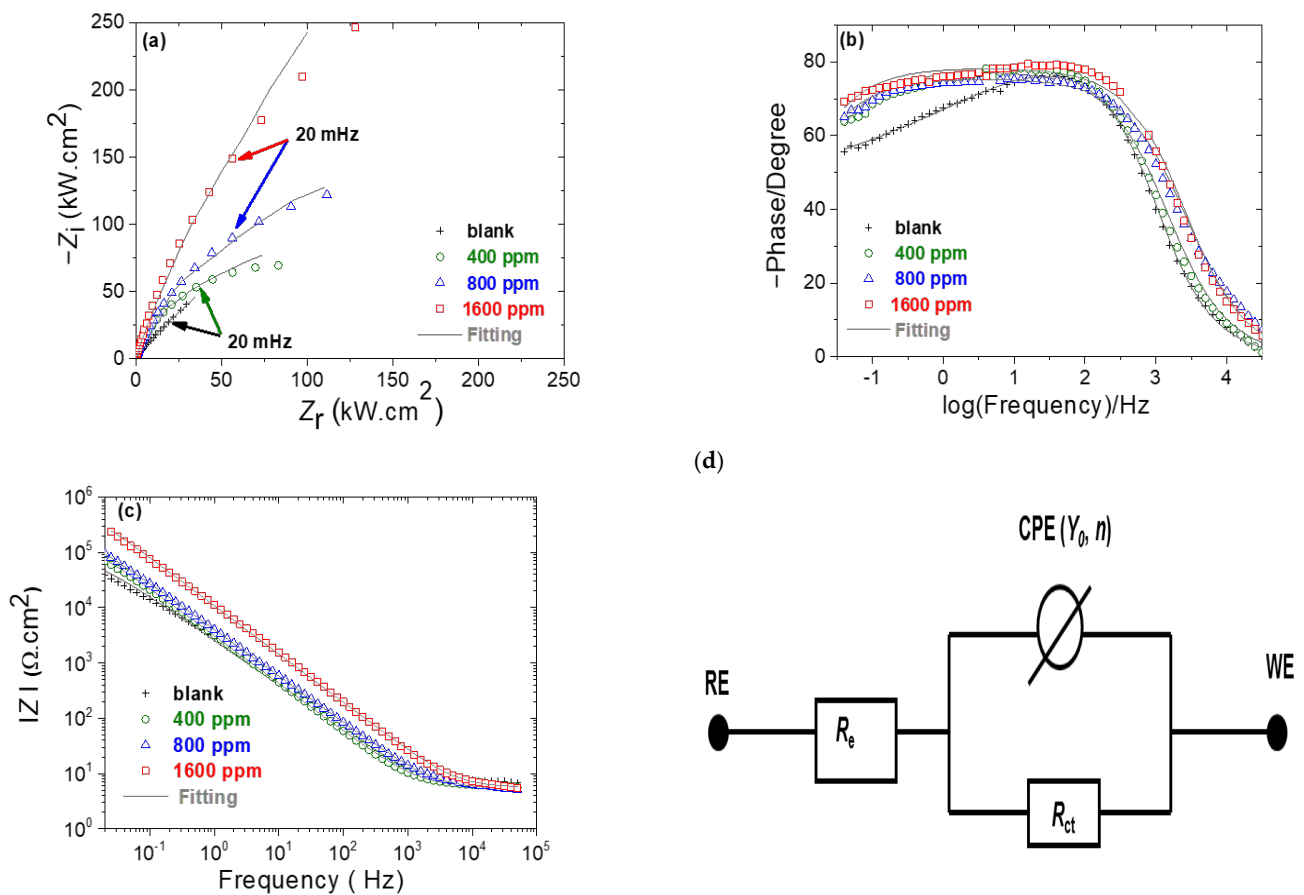


Figure 2. EIS diagrams for 316L stainless steel, after 2 h in 3% NaCl without and with inhibitor, at 25 °C: (a) Nyquist plots, (b) Bode phase angle, (c) Bode modules and (d) Electrical equivalent circuit.

CPE is used as a substitute for the capacitor to fit more accurately the impedance behavior of the electric double layer. The values of double-layer capacitance (C_{dl}) have been calculated from electrolyte resistance and CPE constants (Y_0 and n) using the relationship noted, which is derived from Brug's formula [35] when the electrolyte resistance R_e is much smaller than the transfer resistance R_{ct} .

$$C_{dl} = (Y_0 R_e^{1-n})^{1/n} \quad (\text{when } R_e \ll R_{ct}) \quad (3)$$

A good correlation between experimental and simulated data was obtained (the error of the fitted parameters is calculated by the chi-squared χ^2 , which is included for all adjustments between 0.001 and 0.005).

The values presented in Table 1 show that the value of R_{ct} increases with increasing the concentration of inhibitor as compared to the blank sample. These values indicate the formation of a protective layer at the metal/solution interface. The C_{dl} value decreases with increasing the inhibitor concentration, indicating the decrease in the local dielectric constant and/or the increase in the thickness of the electrical double layer. These values are considered inferior to that of the blank value, which confirms the specific adsorption of the inhibitor at the metal/solution interface [36].

The effectiveness of the inhibition determined from the polarization curves and electrochemical impedance measurements (Table 1) increases with the increase in the inhibitor concentration. These values are in good agreement.

3.5. Influence of Temperature on the Effectiveness of the Inhibitor

Temperature is an important factor that can have an effect on the corrosion phenomena. The measurements have been taken at different temperatures (25–80 °C), in the absence and presence of 1600 ppm of the inhibitor *Thymus satureoides* oil in 3% NaCl.

3.5.1. Potentiodynamic Polarization

The following curves (Figure 3a,b) show the potentiodynamic behavior of 316L stainless steel in a solution of 3% NaCl in the absence and presence of 1600 ppm of the inhibitor at different temperatures.

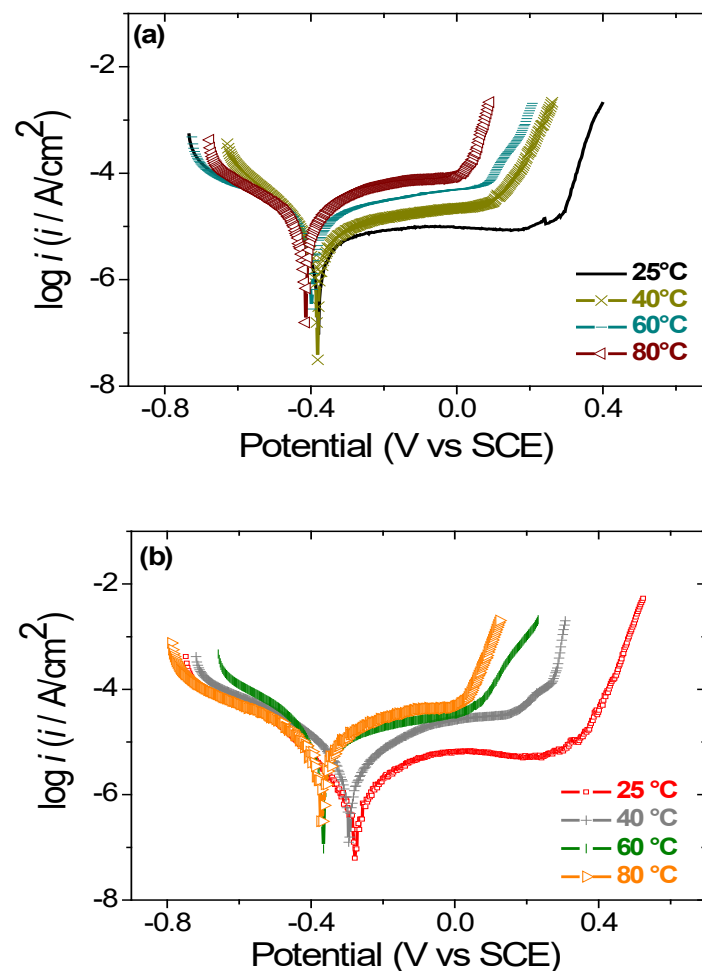


Figure 3. Potentiodynamic polarization curves (scan rate of 0.5 mVs^{-1}) for 316L in 3% NaCl: (a) without and (b) with 1600 ppm inhibitor, at different temperatures.

The electrochemical parameters such as the potential corrosion, the corrosion current density, the passivation current density and the pitting potential obtained using these potentiodynamic polarization curves are shown in Supplementary Material Tables S2 and S3.

Figure 3a,b and Supplementary Material Tables S2 and S3 indicate that there is a general increase in the corrosion rate when increasing the temperature from 25 to 80 °C. The solution becomes more corrosive with the temperature rise and the protective inhibitor power decreases. This implies that this inhibitor is adsorbed on the metal by electrostatic bonds (weak bonds). This type of temperature-sensitive link cannot fight effectively against corrosion with increasing temperature [5,6,9,11].

Additionally, we note that the addition of the inhibitor makes the pitting potential (E_{pit}) shift toward positive values for all temperatures. Therefore the *Thymus satureoides* oil

inhibits pitting corrosion for all studied temperatures, even if the effect is less important with an increase in temperature.

3.5.2. Determination of the Activation Energy (Adsorption Isotherms)

According to some authors [37,38], the logarithm of the corrosion rate (i_{corr}) is a linear function with the inverse of the absolute temperature $1/T$ (Arrhenius equation noted 4):

$$\ln(i_{\text{corr}}) = -\frac{E_a}{RT} + \ln(A) \quad (4)$$

where E_a is the activation energy, T is the absolute temperature, R is the gas constant and A is the pre-exponential factor of the Arrhenius equation, ΔS^* is the activation entropy and ΔH^* is the activation enthalpy.

Some conclusions on the action mechanism of the inhibitors can be obtained by comparing E_a measured both in the presence and in the absence of the corrosion inhibitor. The variation in the corrosion current logarithm as a function of T^{-1} for 316L samples in 3% NaCl in the absence and presence of 1600 ppm of the *Thymus saturooides* oil is represented in Figure 4.

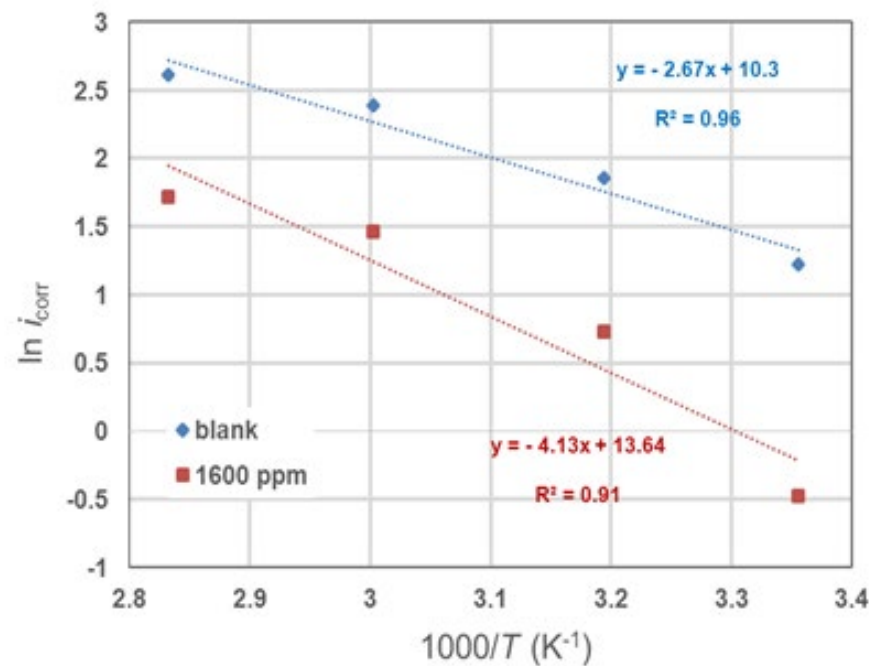


Figure 4. Arrhenius diagrams of 316L dissolution in 3% NaCl with and without inhibitor, at different temperatures.

The variation in the current corrosion logarithm as a function of T^{-1} provides straight lines indicating that the Arrhenius law is respected. The values of the activation energies obtained from these straight lines are, respectively, 22.2 kJmol^{-1} and 34.4 kJmol^{-1} for the solution without and with inhibitor.

It is clear that the presence of the inhibitor increases the activation energy. This behavior demonstrates the phenomenon of physical adsorption of the inhibitor on the metal surface.

The kinetic parameters, the enthalpy and the entropy of the corrosion process are also evaluated from the study of the temperature effect. An alternative formulation of the Arrhenius equation is given by the relationship noted:

$$i_{\text{corr}} = \frac{RT}{Nh} \exp\left(\frac{\Delta S^*}{R}\right) \exp\left(-\frac{\Delta H^*}{RT}\right) \quad (5)$$

where h is the Planck constant, N is the Avogadro number, T is the absolute temperature, R is the gas constant, ΔS^* is the activation entropy and ΔH^* is the activation enthalpy [39]. Figure 5 shows plots of $\ln(i_{\text{corr}}/T)$ as a function of $1/T$. The straight lines are obtained with a slope of $-\Delta H^*/R$ and an interception of $(\ln R/Nh + \Delta S^*/R)$, from which the values of ΔS^* and ΔH^* can be calculated.

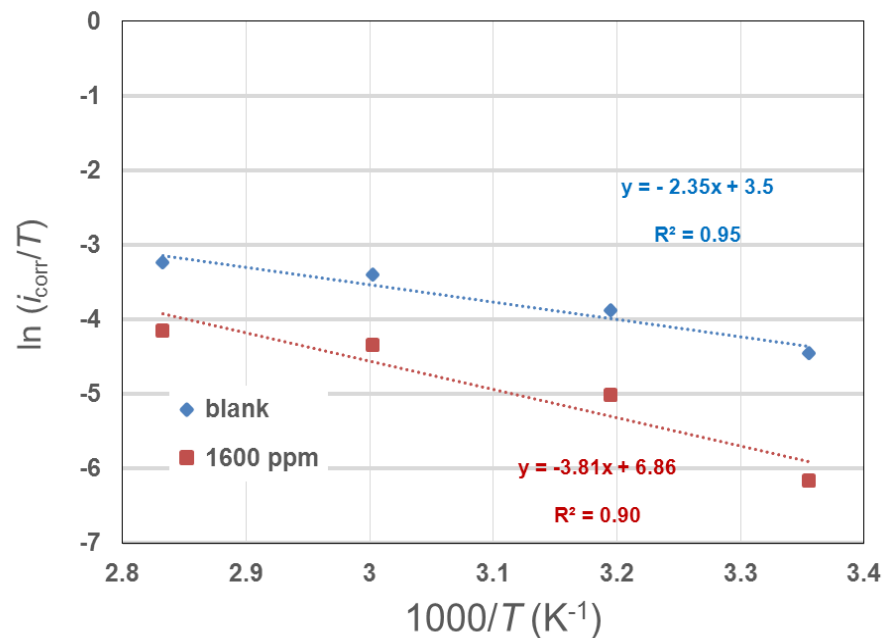


Figure 5. Relations between $\ln(i_{\text{corr}}/T)$ and $1000/T$ at different temperatures.

The activation free energy ΔG^* of the corrosion process at each experimental temperature can be calculated using equation noted 6. The activation parameters values (ΔH^* , ΔS^* and ΔG^*) at 25 °C are given in the Supplementary Material Table S4.

$$\Delta G^* = \Delta H^* - T \times \Delta S^* \quad (6)$$

The positive sign of ΔH^* reflects that the corrosion phenomenon is an endothermic process.

The difference between the two values of entropy ΔS^* shows that the activation entropy is less negative with a great extent of the inhibitor than in its absence. The calculated ΔG^* values are more positive for the inhibited system. They are consistent with the electrostatic interaction between the charged molecules and the charged 316L stainless steel. This fact reflects the formation of a stable layer controlled by the inhibitor physicoadsorption on the surface alloy 316L [39,40].

3.6. AFM and SEM

Steel specimens after immersion for 24 h in 3% NaCl without and with *Thymus sat-ureoides* oil were observed by AFM. The recorded 2D and 3D images of surface topography are shown in Supplementary Material Figure S4.

These images show the rough surface of 316L stainless steel immersed in 3% NaCl and a reduction in surface roughness in the presence of an inhibitor. Supplementary Material Figure S5 shows the calculated difference between the roughness (z) and the mean roughness factor (z^*) noted $(z-z^*)$ corresponding to a profile from the respective 2D images. It is noted that the roughness profile of the steel surface immersed in 3% NaCl solution increased. However, the addition of a 1600 ppm inhibitor decreased the $z-z^*$ factor indicating the adsorption of the inhibitor on the steel surface [31].

These results are confirmed by SEM micrographs (Supplementary Material Figure S6) of 316L stainless steel in 3% NaCl in the absence and presence of a 1600 ppm inhibitor. The

samples were observed after immersion for 24 h. The surface of the polished stainless steel sample (Figure S6a) is very smooth and shows no corrosion while stainless steel dipped in 3% NaCl in the absence of the inhibitor (Figure S6b) is very rough. However, the presence of 1600 ppm decreases the rate of corrosion and the surface damage diminished considerably (Figure S6c) suggesting the formation of a protective inhibitor film at the 316L stainless steel surface [41].

3.7. DFT Study

We have computed the electronic properties of the four majority compounds (Supplementary Material Figure S2), both in the gaseous phase and in water. In order to investigate the possible adsorption sites of these compounds, Figure 6 shows their HOMO (Highest Occupied Molecular Orbital) distribution and Figure 7 their LUMO (Lowest Unoccupied Molecular Orbital) distribution in the gaseous phase and in water.

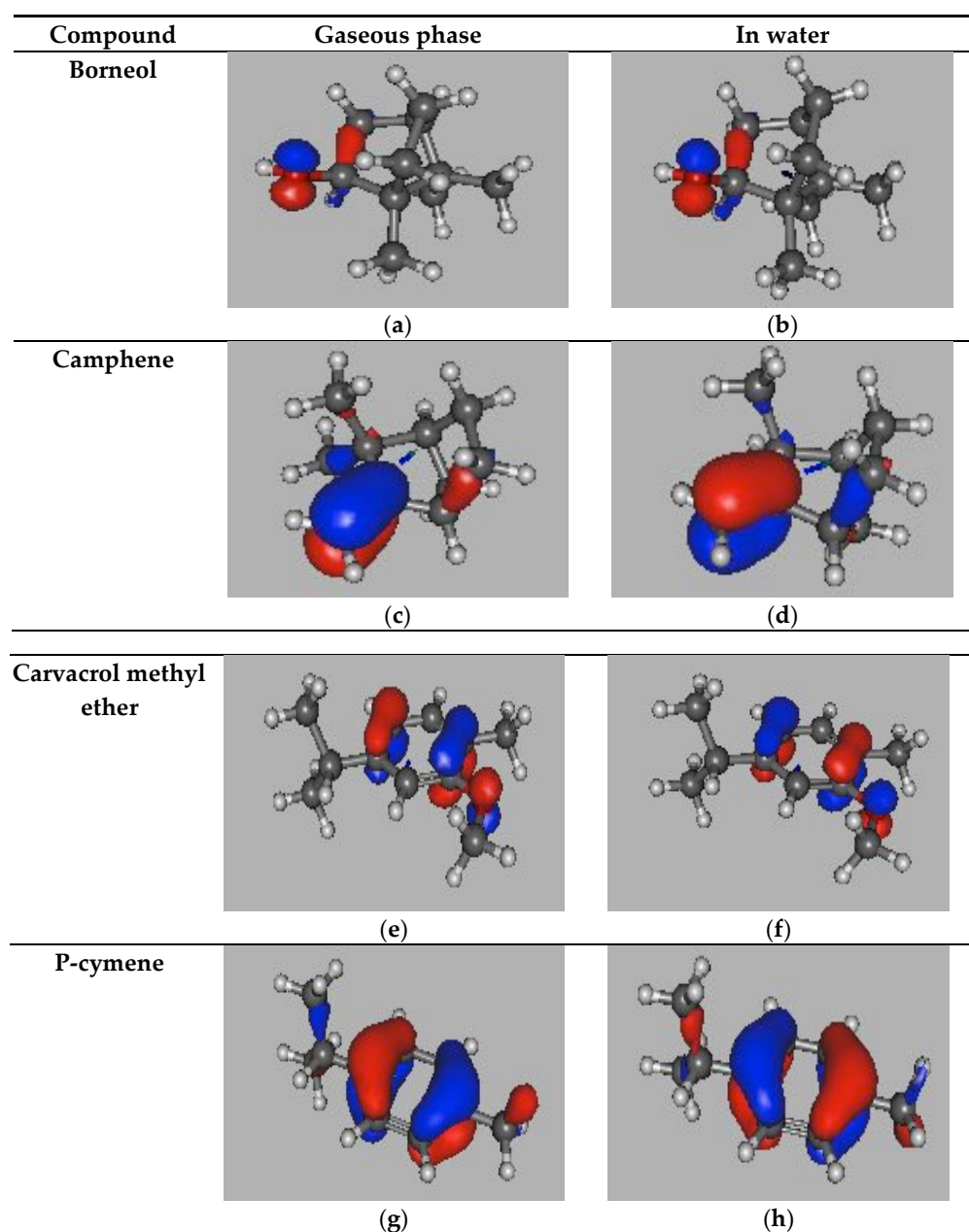


Figure 6. B3LYP HOMO distribution of the four majority compounds: (a,c,e,g) in gaseous phase and (b,d,f,h) in water.

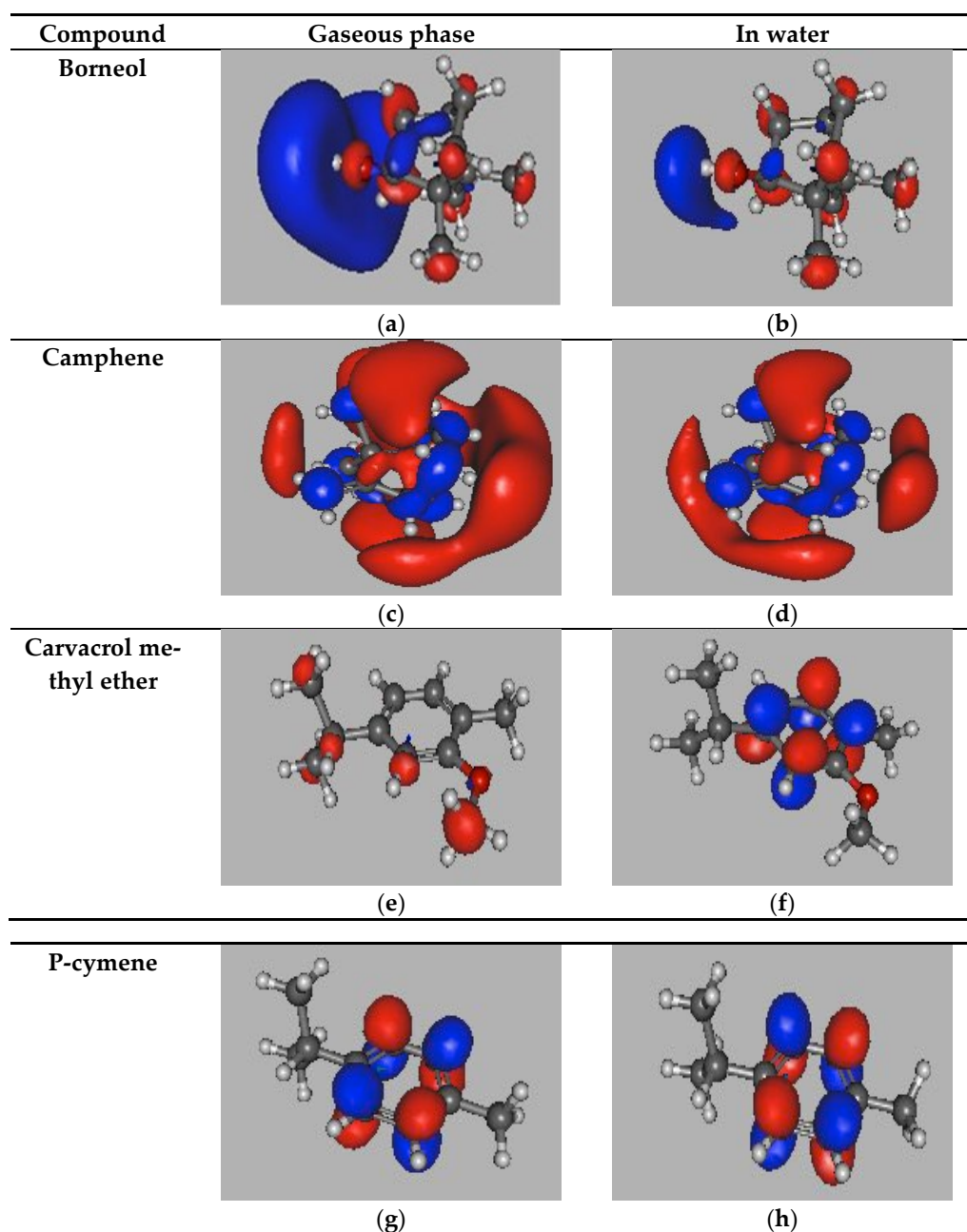


Figure 7. B3LYP LUMO distribution of the four majority compounds: (a,c,e,g) in gaseous phase and (b,d,f,h) in water.

There are very few changes in the distributions between the gaseous phase and solution, except for the LUMO of carvacrol methyl ether. For borneol, the HOMO distribution focuses on the O-H group while the LUMO distribution shows, in addition to the O-H group, a contribution of some CH₃ or CH₂ groups. Thus, the possible adsorption sites on the borneol structure may be mainly the O-H group and, to a lesser extent, some methyl or methylene groups. Regarding camphene, the HOMO distribution focuses on the C=C group while the LUMO distribution shows a large delocalization of the whole molecule. Then, the whole molecule may participate in adsorption. For carvacrol methyl ether, the HOMO distribution is centered on the oxygen atom and the aromatic cycle while the LUMO distribution is located on the aromatic cycle (in water). This last distribution is the same as the one for the molecular orbital immediately above the LUMO in the gaseous phase (difference of 0.1 eV). This inversion is probably due to an artifact at this level of theory.

Thus, the possible adsorption sites on carvacrol methyl ether structure may be the oxygen atom and the aromatic cycle. As for p-cymene, the HOMO and LUMO distributions focus on the aromatic cycle, which may be the possible adsorption site on the p-cymene structure. The corrosion inhibition performance can be evaluated by the energy of the HOMO and the LUMO. The energy of the LUMO characterizes the electron-accepting ability of the inhibitor, and a lower energy value for the LUMO may be better for a corrosion inhibitor. With higher energy of the HOMO, the inhibitor tends to donate electrons and is adsorbed on the metal surface.

Tables 2–4 present the HOMO and LUMO energies of the four majority compounds in the gaseous phase and in water, respectively. In both cases, the highest HOMO corresponds to carvacrol methyl ether. Following the molecule, in the gaseous phase, borneol and p-cymene show the lowest LUMO while in water, it is carvacrol methyl ether (except in BMK for which p-cymene is the one).

Table 2. Energies of the HOMO (Highest Occupied Molecular Orbital) in a gaseous phase and b water.

Functional	B3LYP		BMK		M062X	
	a	b	a	b	a	b
Borneol	−7.35	−7.40	−8.39	−8.44	−9.02	−9.06
Camphene	−6.65	−6.73	−7.50	−7.60	−8.04	−8.14
Carvacrol methyl ether	−5.93	−6.10	−6.69	−6.89	−7.25	−7.45
P-cymene	−6.45	−6.57	−7.23	−7.38	(−7.75) *	(−7.89) *

* We have not obtained a geometry corresponding to a strict energy minimum. One small imaginary frequency remains that we have not been able to remove.

Table 3. Energies of the LUMO (Lowest Unoccupied Molecular Orbital) for the four majority compounds in: a gaseous phase and b water.

Functional	B3LYP		BMK		M062X	
	a	b	a	b	a	b
Borneol	−0.38	−0.26	0.30	0.40	−0.15	−0.04
Camphene	−0.26	−0.20	0.35	0.40	−0.07	−0.02
Carvacrol methyl ether	−0.31	−0.35	0.31	0.36	−0.15	−0.10
P-cymene	−0.37	−0.21	0.36	0.26	(−0.07) *	(−0.06) *

* We have not obtained a geometry corresponding to a strict energy minimum. One small imaginary frequency remains that we have not been able to remove.

Table 4. Energy gap HOMO-LUMO ΔE for the four majority compounds in: a gaseous phase and b water.

Functional	B3LYP		BMK		M062X	
	a	b	a	b	a	b
Borneol	6.97	7.14	8.69	8.84	8.87	9.02
Camphene	6.39	6.53	7.85	8.00	7.97	8.12
Carvacrol methyl ether	5.62	5.75	7.00	7.25	7.10	7.35
P-cymene	6.08	6.36	7.59	7.64	(7.68) *	(7.83) *

* We have not obtained a geometry corresponding to a strict energy minimum. One small imaginary frequency remains that we have not been able to remove.

Therefore, the value of the energy gap HOMO-LUMO (ΔE) provides a measure for the stability of the formed complex on the metal surface. The high inhibition efficiency of a molecule can be attributed to the high value of dipole moment and low value of ΔE [42–44].

Both in the gaseous phase and in water, the carvacrol methyl ether molecule shows the lowest ΔE (Table 4). In order to evaluate the possible influence of hydrogen bonding

for the two oxygenated molecules (borneol and carvacrol methyl ether), we have examined the system “molecule + H₂O” in water. The optimized geometries are shown in Figure 8 and the HOMO and LUMO energies are given in Supplementary Material Table S5. This confirms the lowest ΔE for the carvacrol methyl ether.

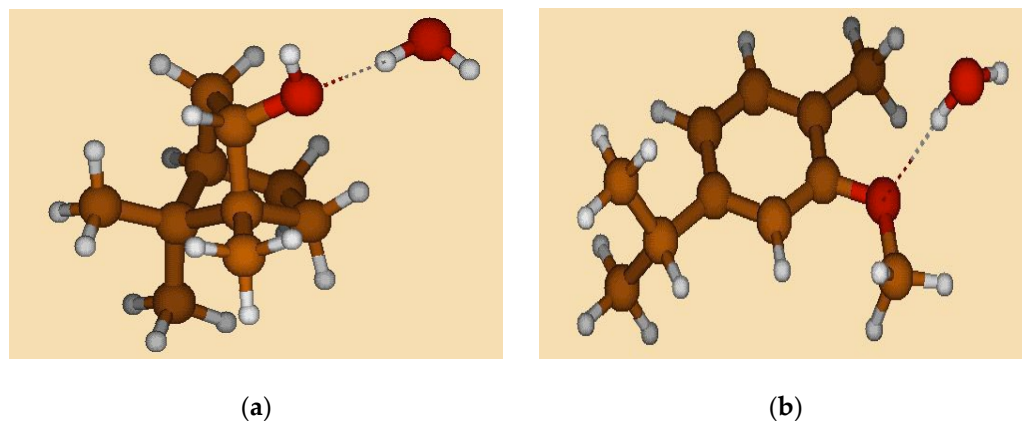


Figure 8. Optimized molecular structure of the two oxygenated compounds: (a) borneol and (b) carvacrol methyl ether in water with one H₂O molecule.

The dipole moment in the gaseous phase for the four majority compounds is presented in Supplementary Material Table S6. Without surprise, borneol and carvacrol methyl ether correspond to the highest dipole moments. Borneol and carvacrol methyl ether seem to be interesting corrosion inhibitors.

4. Conclusions

The following conclusions can be drawn from this study:

- This study shows that the essential oil extracted from *Thymus satureoides* endemic to Morocco provides good protection for 316L in a 3% NaCl solution under severe conditions such as a seawater cooling system. *Thymus satureoides* oil is an effective anodic corrosion inhibitor of 316L stainless steel in a solution of 3% NaCl. The electrochemical measurements show that the efficiency of the inhibitor increases with the concentration and that the corrosion current is reduced by 82% when the concentration reaches a value of 1600 ppm.
- Thermodynamic analyses give evidence that the adsorption of the *Thymus satureoides* oil on stainless steel 316L in 3% NaCl solution is an endothermic physisorption process.
- Physical analyzes by AFM and SEM show a decrease in the roughness of 316L stainless steel samples after corrosion in a saline solution containing 1600 ppm of Thymus oil compared to a solution without an inhibitor. AFM and SEM studies showed a roughness decrease for the 1600 ppm inhibitor.
- Theoretical studies show that carvacrol methyl ether and borneol can be the best inhibitors among all components of *Thymus satureoides* oil, some additional studies may be undertaken separately to analyze their intrinsic properties as stainless steel corrosion inhibitors.

Supplementary Materials: The following supporting information can be downloaded at: <https://www.mdpi.com/article/10.3390/lubricants11020056/s1>, Figure S1: Chromatogram of the *Thymus satureoides* essential oil. Constituents a,q are given in Supplementary Material Table S1; Figure S2: Chemical structure of majority compounds: a borneol, b camphene, c p-cymene and d carvacrol methyl ether; Figure S3: Potential follow-up in open circuit of the stainless steel immersed in 3% NaCl solution without and with the inhibitor; Figure S4: 2D and 3D atomic force micrographs of 316L stainless steel: (a-a') before immersion (polished), (b-b') after immersion in 3% NaCl and (c-c') after immersion in 3% NaCl+1600 ppm during 24 h; Figure S5: Calculated roughness ($z-z^*$) factor for 316L stainless steel: (a) before immersion (polished), (b) after immersion in 3% NaCl and c after immersion in

3% NaCl+1600 ppm inhibitor during 24 h; Figure S6: SEM image of 316L stainless steel: a before immersion (polished), b after immersion in 3% NaCl and c after immersion in 3% NaCl+1600 ppm inhibitor during 24 h; Table S1: Main constituents of the *Thymus satureoides* essential oil; Table S2: Electrochemical parameters (corrosion potential (E_{corr}), corrosion current density (i_{corr}), passivation current density (i_{pass}), pitting corrosion (E_{pit})) of 316L in 3% NaCl without inhibitor at different temperatures; Table S3: Electrochemical parameters (corrosion potential (E_{corr}), corrosion current density (i_{corr}), passivation current density (i_{pass}), pitting corrosion (E_{pit})) of 316L stainless steel in 3% NaCl with 1600 ppm inhibitor at different temperatures; Table S4: The activation parameters values (activation enthalpy (ΔH^*), activation entropy (ΔS^*) and activation free energy (ΔG^*)) of 316L stainless steel in 3% NaCl without and with 1600 ppm of the *Thymus satureoides* oil; Table S5: Energies of the HOMO (Highest Occupied Molecular Orbital) and the LUMO (Lowest Unoccupied Molecular Orbital) of the two oxygenated compounds in water with one H₂O molecule. ΔE is the energy gap HOMO-LUMO; Table S6: B3LYP dipole moment (in Debye) for the four majority compounds in gaseous phase.

Author Contributions: Conceptualization, S.S. and F.S.-L.; software, S.S., F.S.-L. and F.B.; validation J.P.C. and M.E.; formal analysis, L.V., S.S. and F.S.-L.; investigation, S.S. and A.L.; resources, J.P.C. and M.E.; writing—original draft preparation, F.S.-L.; writing—review and editing, F.S.-L. and J.P.C.; supervision, J.P.C.; project administration, M.E. and J.P.C. All authors have read and agreed to the published version of the manuscript.

Funding: This research received no external funding.

Data Availability Statement: Not applicable.

Acknowledgments: This work was financially supported by University Hassan 1er (Morocco) through the grant awarded to Soukaina Slaoui. The authors are grateful to Mickaël Gilliot (MATIM) for AFM discussions and to Jean-Marc Patat (LISM) for SEM/EDXS analyses. The computational center of the University of Reims Champagne-Ardenne (Romeo) is acknowledged for the CPU time donated.

Conflicts of Interest: The authors declare no conflict of interest.

References

1. Sedriks, J. *Corrosion of Stainless Steels*, 2nd ed.; John Wiley & Sons: Hoboken, NJ, USA, 1996; ISBN 978-0-471-00792-0.
2. Fossati, A.; Borgioli, F.; Galvanetto, E.; Bacci, T. Corrosion Resistance Properties of Glow-Discharge Nitrided AISI 316L Austenitic Stainless Steel in NaCl Solutions. *Corros. Sci.* **2006**, *48*, 1513–1527. [[CrossRef](#)]
3. Eddy, N.O. Inhibitive and Adsorption Properties of Ethanol Extract of Colocasia Esculenta Leaves for the Corrosion of Mild Steel in H₂SO₄. *Int. J. Phys. Sci.* **2009**, *4*, 165–171.
4. Scully, J.C. *Corrosion Protection. Principes Fondamentaux*; Elsevier Masson: Amsterdam, The Netherlands, 1997; ISBN 2-225-84777-0.
5. Bouyanzer, A.; Hammouti, B. A Study of Anti-corrosive Effects of Artemisia Oil on Steel. *Pigment Resin Technol.* **2004**, *33*, 287–292. [[CrossRef](#)]
6. Bensabah, F.; Houbairi, S.; Essahli, M.; Lamiri, A.; Naja, J. Chemical Composition and Inhibitory Effect of the Essential Oil from Mentha Spicata Irrigated by Wastewater on the Corrosion of Aluminum in 1 Molar Hydrochloric Acid: Port. *Electrochim. Acta* **2013**, *31*, 195–206. [[CrossRef](#)]
7. Bensabah, F.; Houbairi, S.; Essahli, M.; Lamiri, A.; Naja, J. Chemical Composition and Inhibitory Effect of the Essential Oil from Mentha Spicata Irrigated by Wastewater on the Alkaline Corrosion of Aluminum. *J. Adv. Chem.* **2014**, *11*, 1367–1377. [[CrossRef](#)]
8. Espinoza-Vázquez, A.; Rodríguez-Gómez, F.J.; Mata, R.; Madariaga-Mazón, A.; Ángeles-Beltrán, D. Perezzone as Corrosion Inhibitor for AISI 1018 Steel Immersed in NaCl Saturated with CO₂. *J. Solid State Electrochem.* **2017**, *21*, 1687–1697. [[CrossRef](#)]
9. Chetouani, A.; Hammouti, B.; Benkaddour, M. Corrosion Inhibition of Iron in Hydrochloric Acid Solution by Jojoba Oil. *Pigment Resin Technol.* **2004**, *33*, 26–31. [[CrossRef](#)]
10. Mo, S.; Li, L.J.; Luo, H.Q.; Li, N.B. An Example of Green Copper Corrosion Inhibitors Derived from Flavor and Medicine: Vanillin and Isoniazid. *J. Mol. Liq.* **2017**, *242*, 822–830. [[CrossRef](#)]
11. Rahal, C.; Masmoudi, M.; Abdelhedi, R.; Sabot, R.; Jeannin, M.; Bouaziz, M.; Refait, P. Olive Leaf Extract as Natural Corrosion Inhibitor for Pure Copper in 0.5 M NaCl Solution: A Study by Voltammetry around OCP. *J. Electroanal. Chem.* **2016**, *769*, 53–61. [[CrossRef](#)]
12. Deyab, M.A. Egyptian Licorice Extract as a Green Corrosion Inhibitor for Copper in Hydrochloric Acid Solution. *J. Ind. Eng. Chem.* **2015**, *22*, 384–389. [[CrossRef](#)]
13. El-Haddad, M.N. Chitosan as a Green Inhibitor for Copper Corrosion in Acidic Medium. *Int. J. Biol. Macromol.* **2013**, *55*, 142–149. [[CrossRef](#)]

14. Tan, B.; Lan, W.; Zhang, S.; Deng, H.; Qiang, Y.; Fu, A.; Ran, Y.; Xiong, J.; Marzouki, R.; Li, W. Passiflora Edulia Sims Leaves Extract as Renewable and Degradable Inhibitor for Copper in Sulfuric Acid Solution. *Colloids Surf. A: Physicochem. Eng. Asp.* **2022**, *645*, 128892. [[CrossRef](#)]
15. Tan, B.; Zhang, S.; Cao, X.; Fu, A.; Guo, L.; Marzouki, R.; Li, W. Insight into the Anti-Corrosion Performance of Two Food Flavors as Eco-Friendly and Ultra-High Performance Inhibitors for Copper in Sulfuric Acid Medium. *J. Colloid Interface Sci.* **2022**, *609*, 838–851. [[CrossRef](#)]
16. Verma, C.; Ebenso, E.E.; Bahadur, I.; Quraishi, M.A. An Overview on Plant Extracts as Environmental Sustainable and Green Corrosion Inhibitors for Metals and Alloys in Aggressive Corrosive Media. *J. Mol. Liq.* **2018**, *266*, 577–590. [[CrossRef](#)]
17. Shahid, M. Corrosion Protection with Eco-Friendly Inhibitors. *Adv. Nat. Sci. Nanosci. Nanotechnol.* **2011**, *2*, 043001. [[CrossRef](#)]
18. Tan, B.; He, J.; Zhang, S.; Xu, C.; Chen, S.; Liu, H.; Li, W. Insight into Anti-Corrosion Nature of Betel Leaves Water Extracts as the Novel and Eco-Friendly Inhibitors. *J. Colloid Interface Sci.* **2021**, *585*, 287–301. [[CrossRef](#)]
19. Aslam, R.; Mobin, M.; Zehra, S.; Aslam, J. A Comprehensive Review of Corrosion Inhibitors Employed to Mitigate Stainless Steel Corrosion in Different Environments. *J. Mol. Liq.* **2022**, *364*, 119992. [[CrossRef](#)]
20. Xin, S.S.; Li, M.C. Electrochemical Corrosion Characteristics of Type 316L Stainless Steel in Hot Concentrated Seawater. *Corros. Sci.* **2014**, *81*, 96–101. [[CrossRef](#)]
21. Frisch, M.J.; Trucks, G.; Schlegel, H.; Scuseria, G.; Robb, M.; Cheeseman, J.; Scalmani, G.; Barone, V.; Mennucci, B.; Petersson, A.; et al. Gaussian, Inc., Wallingford CT, 2009. Gaussian 09, Revision A.02. *Phys. Rev. B: Condens. Matter Mater. Phys* **1988**, *37*, 785.
22. McLean, A.D.; Chandler, G.S. Contracted Gaussian-Basis Sets for Molecular Calculations. 1. 2nd Row Atoms, $Z = 11 - 18$. *J. Chem. Phys.* **1980**, *72*, 5639–5648. [[CrossRef](#)]
23. Krishnan, R.; Binkley, J.S.; Seeger, R.; Pople, J.A. Self-consistent Molecular Orbital Methods. XX. A Basis Set for Correlated Wave Functions. *J. Chem. Phys.* **1980**, *72*, 650–654. [[CrossRef](#)]
24. Becke, A.D. A New Mixing of Hartree-Fock and Local Density-functional Theories. *J. Chem. Phys.* **1993**, *98*, 1372. [[CrossRef](#)]
25. Lee, C.; Yang, W.; Parr, R.G. Development of the Colle-Salvetti Correlation-Energy Formula into a Functional of the Electron Density. *Phys. Rev. B* **1988**, *37*, 785–789. [[CrossRef](#)] [[PubMed](#)]
26. Boese, A.D.; Martin, J.M.L. Development of Density Functionals for Thermochemical Kinetics. *J. Chem. Phys.* **2004**, *121*, 3405–3416. [[CrossRef](#)] [[PubMed](#)]
27. Zhao, Y.; Truhlar, D.G. The M06 Suite of Density Functionals for Main Group Thermochemistry, Thermochemical Kinetics, Noncovalent Interactions, Excited States, and Transition Elements: Two New Functionals and Systematic Testing of Four M06-Class Functionals and 12 Other Functionals. *Theor. Chem. Acc.* **2008**, *120*, 215–241. [[CrossRef](#)]
28. Tomasi, J.; Mennucci, B.; Cammi, R. Quantum Mechanical Continuum Solvation Models. *Chem. Rev.* **2005**, *105*, 2999–3094. [[CrossRef](#)]
29. Houbairi, S.; Essahli, M.; Lamiri, A. Inhibition of Copper Corrosion in 2 M HNO₃ by the Essential Oil of Thyme Morocco: Port. *Electrochim. Acta* **2013**, *31*, 221–233. [[CrossRef](#)]
30. Ehsani, A.; Mahjani, M.G.; Hosseini, M.; Safari, R.; Moshrefi, R.; Mohammad Shiri, H. Evaluation of Thymus Vulgaris Plant Extract as an Eco-Friendly Corrosion Inhibitor for Stainless Steel 304 in Acidic Solution by Means of Electrochemical Impedance Spectroscopy, Electrochemical Noise Analysis and Density Functional Theory. *J. Colloid Interface Sci.* **2017**, *490*, 444–451. [[CrossRef](#)]
31. Satapathy, A.K.; Gunasekaran, G.; Sahoo, S.C.; Amit, K.; Rodrigues, P.V. Corrosion Inhibition by Justicia Gendarussa Plant Extract in Hydrochloric Acid Solution. *Corros. Sci.* **2009**, *51*, 2848–2856. [[CrossRef](#)]
32. Azzouyehar, E.; Abu-Obaid, A.; Hajji, M.E.; Bazzi, L.; Belkhaouda, M.; Lamiri, A.; Salghi, R.; Jodeh, S.; Essahli, M. Plants Extract as Green Corrosion Inhibitors: The Case of Eugenol from Clove. *Der. Pharm. Chem.* **2016**, *9*, 467–475.
33. Simescu, F.; Idrissi, H. Corrosion Behaviour in Alkaline Medium of Zinc Phosphate Coated Steel Obtained by Cathodic Electrochemical Treatment. *Corros. Sci.* **2009**, *51*, 833–840. [[CrossRef](#)]
34. Hu, J.-M.; Liu, L.; Zhang, J.-Q.; Cao, C.-N. Electrodeposition of Silane Films on Aluminum Alloys for Corrosion Protection. *Prog. Org. Coat.* **2007**, *58*, 265–271. [[CrossRef](#)]
35. Brug, G.J.; van den Eeden, A.L.G.; Sluyters-Rehbach, M.; Sluyters, J.H. The Analysis of Electrode Impedances Complicated by the Presence of a Constant Phase Element. *J. Electroanal. Chem. Interfacial Electrochem.* **1984**, *176*, 275–295. [[CrossRef](#)]
36. Ituen, E.; Akaranta, O.; James, A.; Sun, S. Green and Sustainable Local Biomaterials for Oilfield Chemicals: Griffonia Simplicifolia Extract as Steel Corrosion Inhibitor in Hydrochloric Acid. *Sustain. Mater. Technol.* **2017**, *11*, 12–18. [[CrossRef](#)]
37. Khadom, A.A.; Yaro, A.S.; Kadum, A.A.H.; AlTaie, A.S.; Musa, A.Y. The Effect of Temperature and Acid Concentration on Corrosion of Low Carbon Steel in Hydrochloric Acid Media. *Am. J. Appl. Sci.* **2009**, *6*, 1403–1409. [[CrossRef](#)]
38. Bouyanzer, A.; Hammouti, B.; Majidi, L. Pennyroyal Oil from Mentha Pulegium as Corrosion Inhibitor for Steel in 1M HCl. *Mater. Lett.* **2006**, *60*, 2840–2843. [[CrossRef](#)]
39. Yurt, A.; Balaban, A.; Kandemir, S.U.; Bereket, G.; Erk, B. Investigation on Some Schiff Bases as HCl Corrosion Inhibitors for Carbon Steel. *Mater. Chem. Phys.* **2004**, *85*, 420–426. [[CrossRef](#)]
40. Bammou, L.; Chebli, B.; Salghi, R.; Bazzi, L.; Hammouti, B.; Mihit, M.; Idrissi, H. Thermodynamic Properties of Thymus Satuireioides Essential Oils as Corrosion Inhibitor of Tinplate in 0.5 M HCl: Chemical Characterization and Electrochemical Study. *Green Chem. Lett. Rev.* **2010**, *3*, 173–178. [[CrossRef](#)]
41. EL-Haddad, M.N. Hydroxyethylcellulose Used as an Eco-Friendly Inhibitor for 1018 c-Steel Corrosion in 3.5% NaCl Solution. *Carbohydr. Polym.* **2014**, *112*, 595–602. [[CrossRef](#)]

42. Bereket, G.; Hür, E.; Öğretir, C. Quantum Chemical Studies on Some Imidazole Derivatives as Corrosion Inhibitors for Iron in Acidic Medium. *J. Mol. Struct. THEOCHEM* **2002**, *578*, 79–88. [[CrossRef](#)]
43. Fang, J.; Li, J. Quantum Chemistry Study on the Relationship between Molecular Structure and Corrosion Inhibition Efficiency of Amides. *J. Mol. Struct. THEOCHEM* **2002**, *593*, 179–185. [[CrossRef](#)]
44. Zhao, P.; Liang, Q.; Li, Y. Electrochemical, SEM/EDS and Quantum Chemical Study of Phthalocyanines as Corrosion Inhibitors for Mild Steel in 1mol/l HCl. *Appl. Surf. Sci.* **2005**, *252*, 1596–1607. [[CrossRef](#)]

Disclaimer/Publisher's Note: The statements, opinions and data contained in all publications are solely those of the individual author(s) and contributor(s) and not of MDPI and/or the editor(s). MDPI and/or the editor(s) disclaim responsibility for any injury to people or property resulting from any ideas, methods, instructions or products referred to in the content.